Article

Anticrossing and Mode Coupling in Bent All-Glass Leakage Channel Microstructured Optical Fibers with Large Mode Area

Alexander N. Denisov [1,*], Vladislav V. Dvoyrin [2] and Sergey L. Semjonov [1]

1   Prokhorov General Physics Institute of the Russian Academy of Sciences, Dianov Fiber Optics Research Center, 119333 Moscow, Russia; sls@fo.gpi.ru

2   Aston Institute of Photonic Technologies, Aston University, Birmingham B4 7ET, UK; v.dvoyrin@aston.ac.uk

*   Correspondence: denisov@fo.gpi.ru

Abstract: This paper presents the results of a detailed theoretical study of the bending properties of original all-glass leakage channel microstructured optical fibers (LC MOFs) over a bending radius range from 3 cm to 11 cm. These LC MOFs contain two layers of fluorine-doped silica glass elements with reduced refractive index, different diameters, and different distances between them. We determined the spatial distributions of the electric field components of different modes in addition to the usual parameters such as effective refractive indices, bending losses, and spatial intensity distributions. A detailed analysis showed that three modes for each polarization have to be considered to correctly calculate the bending losses. Two pairs of these three modes couple in two distinct bending radius ranges, specifically near 3.68 cm and near 5.95 cm, and the mode coupling in these pairs is resonant. The resulting bending losses of the LC MOF for two polarizations are very close to each other and have two maxima at bending radii of 3.68 cm and 5.95 cm. However, the nature of these maxima is not resonant; they are caused by the combined influence of all three modes, each of which has specific dependencies of losses and other parameters on the bending radius that exhibit quasi-resonant behavior near the corresponding bending radii.

Keywords: microstructured optical fiber; photonic crystal fiber; large-mode-area fiber; leakage channel fiber; mode coupling; anticrossing

1. Introduction

Continuous fiber lasers with a power range of several kW are widely used in a variety of applications, including fundamental science, industrial material processing, and medicine [1–5]. The basic elements of these lasers are active single-mode fibers with a large mode area, which should have low bending losses to ensure the compactness of the lasers. At the same time, research continues in the field of passive single-mode optical fibers with a large mode area, which is necessary for the delivery of laser radiation to the required distance with the required beam parameters. Various types of microstructured optical fibers (MOFs), including photonic band-gap fibers [6–8], Bragg fibers [9–11], and leakage channel fibers (LCFs) [12–14], can be used for these applications in addition to traditional optical fibers with a stepped refractive index profile. However, to date, only MOFs with a photonic band gap have been successfully used in continuous fiber lasers with powers greater than 1 kW [1,5]. However, the authors of [5] during the experiments had to significantly increase the diameter of the aluminum coil, on which the active fiber was wound, up to 70 cm instead of 20 cm. This was due to unexpectedly high bending losses, the reason for which is not yet clear and is under investigation. But this result still does not allow for the creation of a sufficiently compact high-power fiber laser based on such an MOF.

MOFs with leakage channels (LC MOFs) have a rather simple geometrical structure, which makes it fairly easy to select their parameters to achieve an effective single-mode

regime at a large core diameter while at the same time providing low bending losses. A characteristic feature of LC MOFs is a non-zero level of losses for all modes, including fundamental ones, and at the same time, these MOFs can achieve an effective single-mode regime, the criterion of which is low leakage losses for two polarizations of fundamental modes (FMs) and simultaneously high leakage losses for higher-order modes (HOMs). At the same time, for use in high-power continuous fiber lasers, only all-glass MOFs can be used, the cladding of which is formed with elements of fluorine-doped silica glass with a reduced refractive index [15,16] instead of air holes. However, the variants of such all-glass MOFs studied so far [15,16] were based on a hexagonal structure and hence have very limited possibilities of varying their parameters and obtaining the required characteristics. This is explained by the use of the stack and draw technique for manufacturing the preforms for these MOFs from rods of different composition. In the theoretical work [15] for the LCF7 sample, the authors managed to achieve a bending-loss level of about 0.5 dB/m for a bending radius of 0.15 m, but only when bending in one of the directions; however, when bending in the orthogonal direction, these losses were higher by an order of magnitude and were about 5 dB/m. Since in practice it is impossible to strictly control the orientation of the internal structure of an MOF with respect to the bending direction, the average value of leakage losses for such an MOF will be very high. The method of drilling holes in pure silica rods with subsequent insertion of fluorine-doped silica rods into them and drawing such a preform into an MOF with the required parameters can give much more possibilities.

We proposed the original design of all-glass LC MOFs with two layers of circular fluorine-doped silica glass elements with reduced refractive index, different diameters, and different closest element distances [17,18]. As calculations have shown, for this LC MOF with a core diameter of 20 μm and certain selected parameters, the spectral range of the effective single-mode regime at a bending radius of 8 cm is from 0.92 μm to 1.21 μm [18]. At the same time, the leakage losses for FMs at a wavelength of 1.05 μm are 0.064 dB/m, and the leakage losses for HOMs exceed 18.6 dB/m, i.e., the loss ratio exceeds 290. The core diameter of 20 μm was chosen because recent studies have shown that fibers with a core diameter of about 20 μm are optimal for use in high-power continuous fiber lasers, providing kilowatts of power at a length of about 10 m [19,20].

Our experimental investigations of the fabricated LC MOFs show that the measured losses for a sample with a core diameter of 22.5 μm at a bending radius of 10 cm in a free coil were less than 0.1 dB/m in the wavelength range from 0.9 to 1.5 μm [18]. It is important to note that, in order to achieve a single-mode operation with minimal bending losses, a coil with a radius of 10 cm was utilized in our studies rather than the calculated value of 8 cm for the model LC MOF structure. It is assumed that this increase in the coil radius was due to some discrepancies between the parameters of the fabricated LC MOF and those of the model structure. However, further detailed studies are needed to better understand the physical mechanisms governing the bending losses of this LC MOF, which were performed in the present work.

Previously, bending losses have been studied for various types of optical fibers [21–23]. In particular, for chalcogenide negative curvature fibers with a hollow core, two maxima were found in the loss dependences on the bending radius [22]; similar dependences with two maxima were observed in calculations for chalcogenide all-solid anti-resonant fibers [23]. Very similar dependences of bending losses on the bending radius were observed for LC MOFs, but with only one loss maximum [24,25]. The observed variations in the bending losses of these fibers were explained by the coupling of the fundamental core modes to the leaked cladding modes [21–25]. No physical mechanisms that could explain such coupling of these modes were given, except for a very schematic diagram in [25] illustrating the supposed coincidence of the real parts of their effective refractive indices (index-matched coupling [26,27]). However, the simple coincidence of the effective refractive indices of the core and cladding modes is not a compelling argument. These modes are localized in different parts of the optical fibers, in the core and in the cladding, respectively. From a physical standpoint, it is unclear how they can interact with each other

and thus be coupled. This can be confirmed by a simple example: in multi-core optical fibers, the refractive index profile is the same for each core, and the fundamental modes have the same effective refractive index; however, the modes are independent. Another issue is the spatial intensity distributions of modes obtained from calculations that show separate intensity maxima in both the core and cladding of the optical fiber. Although the spatial intensity distribution from the calculations corresponds to a specific value of the effective refractive index (real and imaginary parts) and thus represents a specific mode belonging to the entire optical fiber, it is sometimes suggested that these individual maxima represent separate modes.

An interesting structure of an MOF with two layers of holes and two cores was proposed in [27]. In addition to the central core, this MOF had a ring core located between the hole layers. And its parameters were chosen by modeling the central core and the ring core separately with the help of two auxiliary MOFs. Namely, the parameters of the structure of these auxiliary MOFs were chosen such that the real parts of the effective refractive indices for these two structures (the higher-order mode LP_{11} of the core of the first MOF and the ring-core mode of the second MOF) were equal. According to the authors of [27], a resonant increase in the leakage loss of the proposed MOF was obtained for the higher-order mode LP_{11} of the central core due to its coupling with the leaking ring-core mode. The approach proposed by the authors of [27] can assist in finding the MOF structural parameters that result in increased leakage loss for the higher-order mode. But it is evident that the calculated spatial intensity distribution of the MOF mode presented in [27] has a specific value of the effective refractive index (real and imaginary parts) and thus represents a specific mode inherent to this MOF. In other words, due to the resonance influence of the structural parameters of this MOF, the mode in question exhibits a complex spatial intensity distribution with two distinct maxima: in the central core and in the ring core, resulting in an increased leakage loss. Furthermore, this mode is no longer consistent with the LP_{11} type, as it exhibits a complex intensity profile with two maxima.

Interesting and rather detailed theoretical studies of the negative-curvature hollow-core chalcogenide fiber were described in [22]. In their paper, the authors gave the dependences of the real parts of the effective refractive indices on the bending radius for six modes, with three modes for each of the two polarizations. These dependences have a characteristic anticrossing behavior at bending radii of about 5.7 and 9.4 cm, where the effective refractive indices of the two mode pairs for each polarization are maximally close. However, the spatial distributions of the mode intensities for these bending radii were given only for one of the two modes for each polarization and only for two values of the bending radii (5.7 and 9.4 cm), but the evolution of the modes with changing radii was not shown. At the same time, the authors of [22] distinguished in these spatial intensity distributions of modes separate local intensity maxima—in the core and in the capillaries—and attributed them to the fundamental mode of the core and the capillary mode, respectively, which, in their opinion, are coupled to each other. At the same time, it is clear that the given spatial intensity distributions were obtained for a certain value of the effective refractive index, i.e., they refer to a certain mode of this fiber as a whole. Also, the authors of [22] in their paper gave calculated bending losses for two polarizations, which have two maxima at bending radii of about 5.7 and 9.4 cm. However, the authors of [22] did not explain how they obtained only two dependencies of the bending losses on the bending radius for a total of six modes.

Although it was proposed about 20 years ago that in various optical fibers the core modes are coupled to some cladding modes [21,26], no compelling physical evidence has been presented to support this hypothesis. Nevertheless, this theory is still widely accepted today and is practically taken for granted [23]. Therefore, a more detailed theoretical analysis of the bending characteristics of the LC MOF is one of the objectives of the present work.

The coupled-mode theory has been widely used for more than 50 years and has been applied to theoretical studies of distributed feedback lasers [28], as well as to theoretical

studies of the propagation and interaction of optical radiation in dielectric waveguides [29]. Also, this theory was used for the modeling of various optical fiber gratings [30–36] and for the estimation of radiation propagation losses in two-dimensional photonic crystal waveguides [37]. All these works are characterized by the presence of longitudinal inhomogeneity in the investigated fibers and waveguides, which, in fact, determines the coupling of modes.

It is important to note that, as referenced in [38], coupled-mode theory is a phenomenological theory that relies on fitted coupling coefficients and lacks a foundational validation based on electromagnetic principles. In their study, the authors of [38] employed an ab initio Maxwellian approach with quasinormal-mode theory to derive an "exact" Maxwell evolution (EME) equation for resonator dynamics. They anticipate that this new EME equation will be applicable to all geometries of electromagnetic resonators and that their theoretical approach can be extended to other areas of wave physics.

An interesting method for mode control and tuning in anisotropic optical microresonators with whispering gallery modes (WGMs) was proposed in [39]. In these resonators, anticrossings (and couplings) of different modes occur regularly, but this effect is poorly understood and harmful for mode control and tuning. Uncertainty with the anticrossing behavior is greatly due to the dominant view of WGMs as scalar modes obeying the scalar Helmholtz equation. The authors of [39] have shown that the anticrossings are inherent in the o- and e-modes because of the vectorial properties of Maxwell's equations. Using the electric field component E_z and the magnetic field component H_z as a pair of independent variables and a novel perturbative approach employing a strong localization of the modes near the resonator rim, they quantified the anticrossings. The inferred values of the avoidance gaps were confirmed experimentally in resonators made of lithium niobate. Based on the expected properties of anticrossings, the authors of [39] introduced a mode-control method to get rid of unwanted WGMs. As a result, they eliminated the destructive effect of anticrossings on frequency hopping.

A detailed theoretical study of anticrossing and mode coupling in a bent LC MOF, such as that in [39], appears to be quite challenging due to its geometrical structure. Nevertheless, Maxwell's equations are fundamental and are the basis of much of the software for numerical calculations. Therefore, in the present work, we set out to follow the variations in the spatial distributions of the electric and magnetic field components of different modes as the bending radius of the LC MOF changes. Together with the usual parameters such as effective refractive indices, bending losses, and spatial intensity distributions, this allowed us to interpret the results of the numerical calculations in a more physically justified way. It was also important to perform the calculations in as much detail as possible in order to correctly interpret the results, which were given special attention in the present work.

We have previously carried out studies of the bending losses in the LC MOF, in which we found a maximum loss at a bending radius of approximately 6 cm [17]. In reality, however, the presence of this maximum was explained by the existence of two individual modes for each polarization and different dependencies of their losses on the bending radius in the region near 6 cm: an increase or decrease for different modes. In [17], the minimum loss from these two modes was selected as an approximate estimation of the LC MOF losses, a fact that was explicitly stated in the aforementioned reference. One of the aims of this paper was to perform a more accurate calculation of the bending losses, in contrast to the relatively approximate estimates that have been previously reported.

In the present work, we present the results of a detailed theoretical (numerical) study of the bending properties of all-glass LC MOFs across a range of bending radii from 3 cm to 11 cm. In addition to the usual parameters, such as effective refractive indices, bending losses, and spatial intensity distributions, we determined the spatial distributions of the electric field components of different modes. A comprehensive examination revealed that a physically accurate interpretation of the numerical results requires the consideration of three real modes for each polarization. These modes have a complex spatial intensity

distribution, with maxima both in the LC MOF core and in the ring gap between the element layers. It should be noted that the maxima in the ring gap have different shapes for different modes. It is also crucial to consider three real modes for precise bending-loss calculations. Two pairs of these three modes are coupled in two different bending radius ranges, namely near 3.68 cm and near 5.95 cm. The coupling of the modes in these pairs is resonant. The resulting bending losses of the LC MOF have two maxima at bending radii of 3.68 cm and 5.95 cm, but this is due to the joint influence of all three modes, each of which has specific dependences of its losses and intensity on the bending radius that exhibit quasi-resonant behavior near the corresponding bending radii.

2. Materials and Methods

This LC MOF has a pure silica glass core with a diameter of D_{core} and a cladding containing two rings of circular elements of fluorine-doped silica glass with a reduced refractive index, different diameters, and different spacings between them (Figure 1).
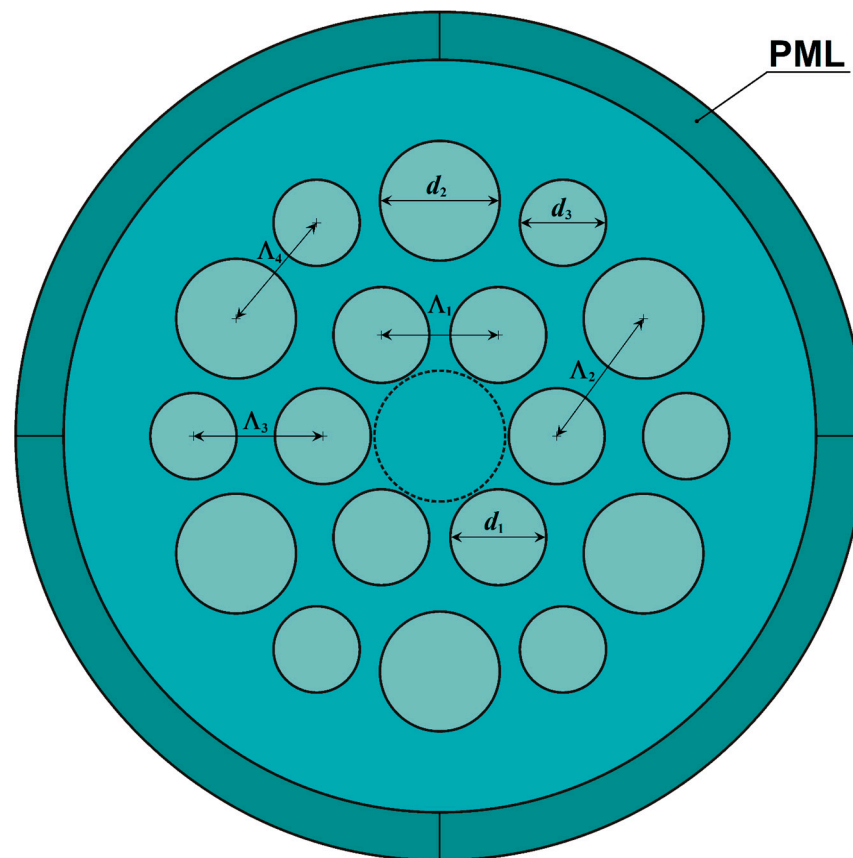

Figure 1. Structure of MOF-18: d_1/Λ_1 = 0.82; d_2/d_1 = 1.25; d_3/d_1 = 0.90; Λ_2/Λ_1 = 1.25; and Λ_3/Λ_1 = 1.10.

The ring gap between the first and second rings is the key feature of this design. It lets us increase leakage losses for higher-order modes (HOMs) compared to fundamental modes (FMs), creating a single-mode regime. The first ring of the cladding comprises six identical circular elements with a diameter of d_1, situated at a distance of Λ_1 from one another. The twelve elements of the second ring of the cladding have different diameters ($d_2 > d_1$ and $d_3 \leq d_2$) and also different distances from the elements of the first ring (Λ_2 and Λ_3). Such LC MOF structure offers a high degree of flexibility in modifying its parameters (d_1, d_2, and d_3, as well as Λ_1, Λ_2, and Λ_3) in order to enhance MOF performance, particularly in increasing leakage losses for HOMs compared to FMs. The optimal ratio of LC MOF parameters for a specific problem can be determined through a multi-objective

optimization algorithm. However, even with the assistance of a supercomputer, this process may necessitate continuous counting for several weeks [40].

In the paper of [18], we opted for a relatively straightforward objective: achieving a single-mode regime in the spectral region around λ = 1.05 µm for LC MOF with a core diameter of D_{core} = 20 µm at a fixed ratio of element diameters (d_2/d_1 = 1.15, d_3/d_1 = 1.00), and with a bending radius down to 8 cm. The remaining LC MOF structure parameters were determined to meet the effective single-mode criteria [12]: low leakage losses for FMs (less than 0.1 dB/m) and simultaneously high leakage losses for HOMs (greater than 1.0 dB/m) over a spectral range of at least 1.0 µm to 1.1 µm, with two orthogonal bending directions considered. Accordingly, the following parameters were selected for calculating the LC MOF characteristics: d_1/Λ_1 = 0.795, Λ_2/Λ_1 = 1.226, and Λ_3/Λ_1 = 1.103 [18].

We used the same parameters for calculations as in [18]. A pure silica glass has a refractive index of n_{sil}, which was determined using the Sellmeier equation [41] (p. 6). For fluorine-doped silica glass elements, we used the refractive index to be $n_{fls} = n_{sil} - 4 \times 10^{-3}$. This variant is called MOF-18, where 18 is the total number of elements [18]. Note that the MOF-18 variant shown in Figure 1 has other parameters that were chosen for clarity.

For calculations of leakage losses of the bent MOF-18, we used a model straight MOF-18 with an equivalent refractive index profile, n_{equ}, which was determined using one of the simplest expressions [42]:

$$n_{equ}(x,y) = n(x,y)\left(1 + \frac{x}{R}\right),\tag{1}$$

where $n(x,y)$ is the original refractive index profile of straight MOF-18, and R is the bending radius in meters. Figure 2 shows the spatial distribution of n_{equ} across the MOF-18 cross section for R = 0.03 m.

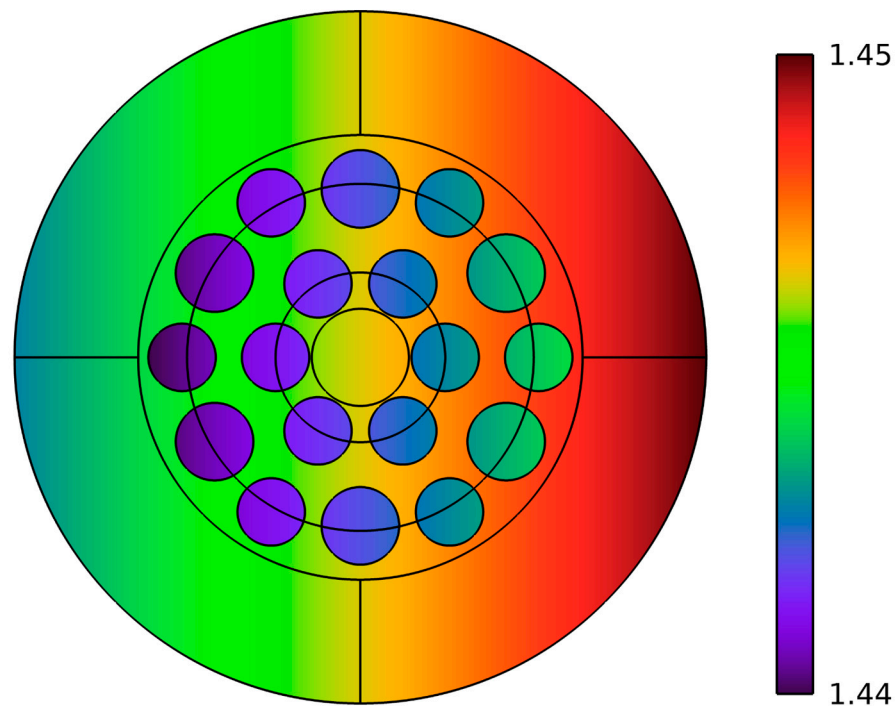**Figure 2.** Spatial distribution of n_{equ} across the MOF-18 cross section for R = 0.03 m.

Previously, we have noted that, with the parameters chosen, MOF-18 has very similar parameters for bending along the x-axis and along the y-axis, including the bending losses [17]. Therefore, only bending along the *x*-axis will be considered in this paper.

3. Calculation Results

The MOF-18 characteristics were numerically calculated by the finite element method (FEM) with a cylindrical perfectly matched layer (PML) for a wavelength of 1.05 μm. In Figure 1, the PML is schematically shown with a dark cyan ring. The actual PML width is displayed in Figure 2 and was determined by the COMSOL 6.0 software algorithm described in the package manual, "Leaky Modes in a Microstructured Optical Fiber", for each bending radius and appropriate effective refractive index range.

Figure 3 shows the dependence of the effective refractive indices of MOF-18 Modes 1a, 1b, and 1c on the bending radius R. The numbers 1 and 2 denote the modes polarized along the x-axis and along the y-axis, respectively. The letters "a", "b", and "c" denote the modes in descending order of the real part of their effective refractive indexes.
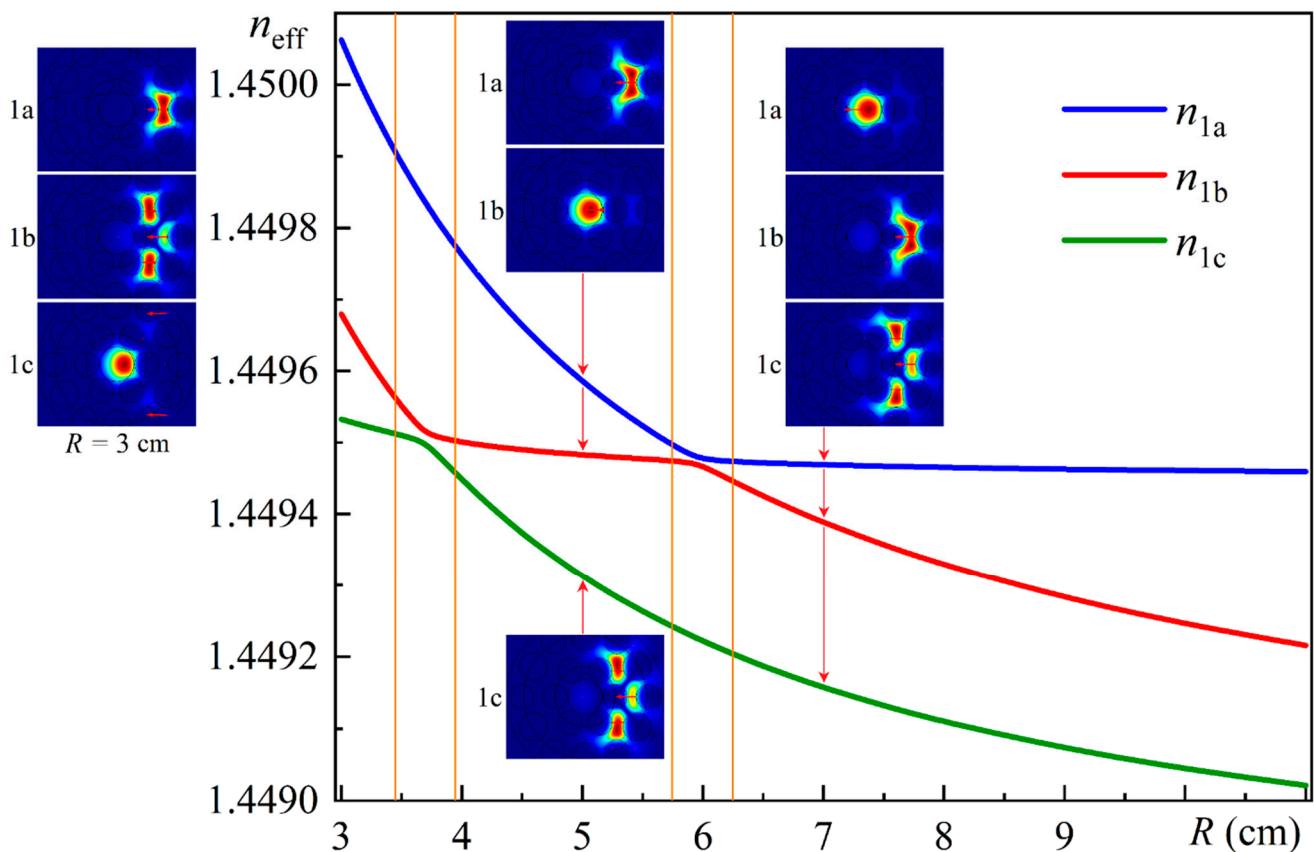

Figure 3. Dependences of the effective refractive indices of MOF-18 Modes 1a, 1b, and 1c on the bending radius R. Insets—spatial intensity distributions of Modes 1a, 1b, and 1c for bending radii of 3.0 cm, 5.0 cm, and 7.0 cm; red arrows indicate direction and relative magnitude of electric field.

The insets in Figure 3 show the spatial intensity distributions of Modes 1a, 1b, and 1c for bending radii of 3 cm, 5 cm, and 7 cm. As can be seen from these insets, Modes 1a, 1b, and 1c for bending radii of 7 cm, 5 cm, and 3 cm, respectively, look similar to the fundamental modes of MOF-18. Accordingly, these modes may be classified as LP_{01} types for their respective bending radii. But a closer look reveals that they also have additional maxima in the ring gap with relatively low intensities. In contrast, the other two modes for these bend radii have the main intensity peaks in the ring gap (with different shapes for different modes) but also have an additional maximum in the core of MOF-18 with relatively low intensity.

Figure 4 shows the differences in the effective refractive index for different pairs of orthogonal modes of MOF-18 as a function of bending radius R. Considering the substantially different y-axis scales in Figures 3 and 4, it becomes clear that the plots for orthogonal

modes in Figure 3 should practically coincide. As can be seen from Figure 3, for a radius of 5.95 cm, the difference in the effective refractive index between Modes 1a and 1b reaches a minimum, approximating 10^{-5}. As illustrated in Figure 4, for radii within the range of 4 cm to 11 cm, the differences in the effective refractive index for Modes 1a and 2a, as well as for Modes 1b and 2b, are less than 4×10^{-7}, which is approximately 25 times less than 10^{-5}. This is also true for other parameters of MOF-18. Therefore, all illustrations in this paper pertain to Modes 1a, 1b, and 1c only.
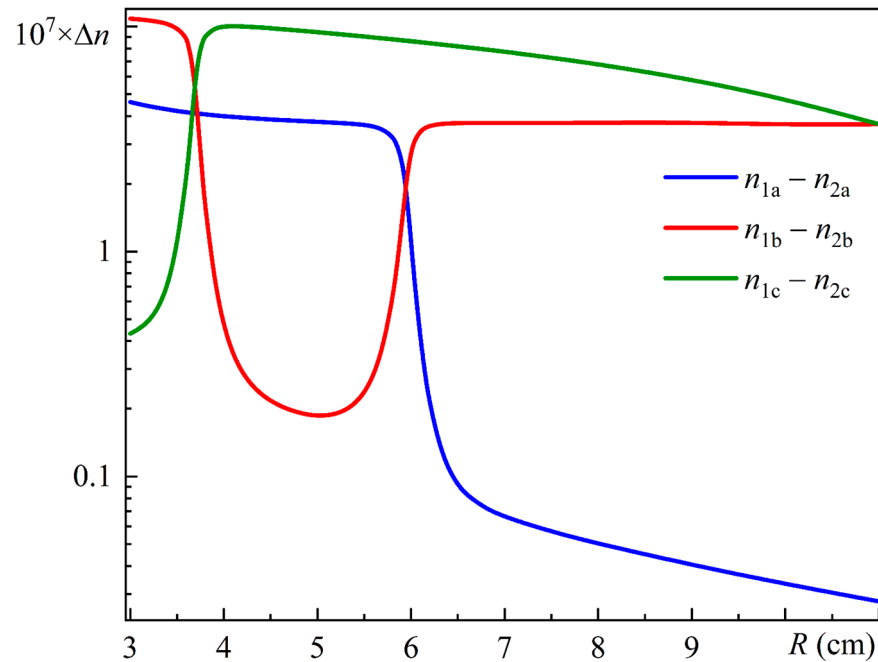
Figure 4. Differences in effective refractive index for different pairs of orthogonal modes of MOF-18 as a function of bending radius *R*.

The most significant transformations of Modes 1a, 1b, and 1c occur in relatively narrow intervals of bending radius variation: from 5.70 cm to 6.25 cm for Modes 1a and 1b, and from 3.50 cm to 3.90 cm for Modes 1b and 1c, as shown in Figure 5. These intervals are marked in Figure 3 by orange vertical lines, which also allow us to clearly identify them as the regions in which the effective refractive indexes of these different pairs of modes become very close.

As seen in Figure 5a for a bending radius of 5.95 cm, Modes 1a and 1b have very close spatial intensity distributions (in the core and in the ring gap) and also have very close effective refractive indices (see Figure 3). Furthermore, as seen in Figure 5b for a bending radius of 3.68 cm, Modes 1b and 1c have very close spatial intensity distributions (in the core and in the ring gap) and also have very close effective refractive indices. In general, the observed variations in the effective refractive indices shown in Figure 3 are characteristic of cases of mode coupling and have the so-called anticrossing character. One of the parameters that characterizes the coupling of modes is the avoidance gap [39]. In our case, it is the difference between the effective refractive indices of the corresponding modes.

Figure 6 shows differences in effective refractive indices for different pairs of modes of MOF-18 as a function of bending radius *R*. As can be seen from Figure 6, the refractive index difference of Modes 1a and 1b reaches a minimum at a bending radius of MOF-18 of about 5.95 cm and is about 10^{-5}. For Modes 1b and 1c, the refractive index difference reaches a minimum at a bending radius of 3.68 cm and is slightly less than 2×10^{-5}. The positions of these minima correspond to MOF-18 bend radius values where the corresponding modes have very close spatial intensity distributions, as shown above (Figure 5). At the same time, their magnitudes give an indication of the degree of coupling between these modes.
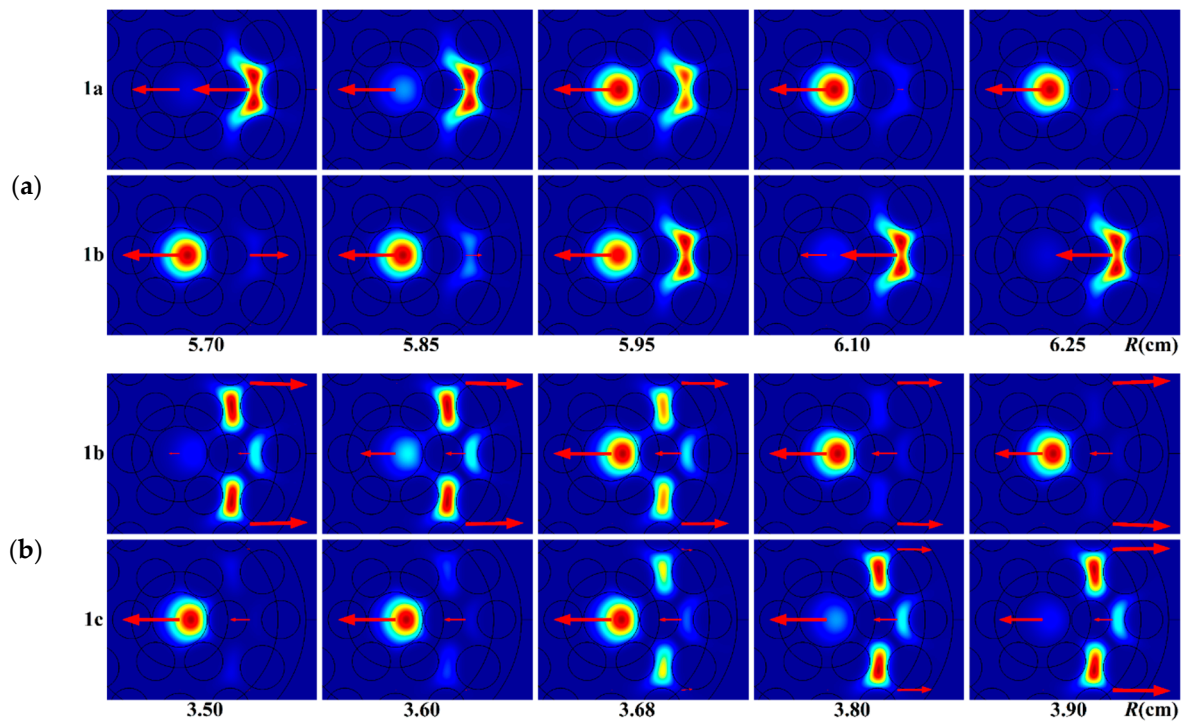
Figure 5. (**a**) Spatial intensity distributions of Modes 1a and 1b for bending radii from 5.70 cm to 6.25 cm; (**b**) spatial intensity distributions of Modes 1b and 1c for bending radii from 3.50 cm to 3.90 cm.
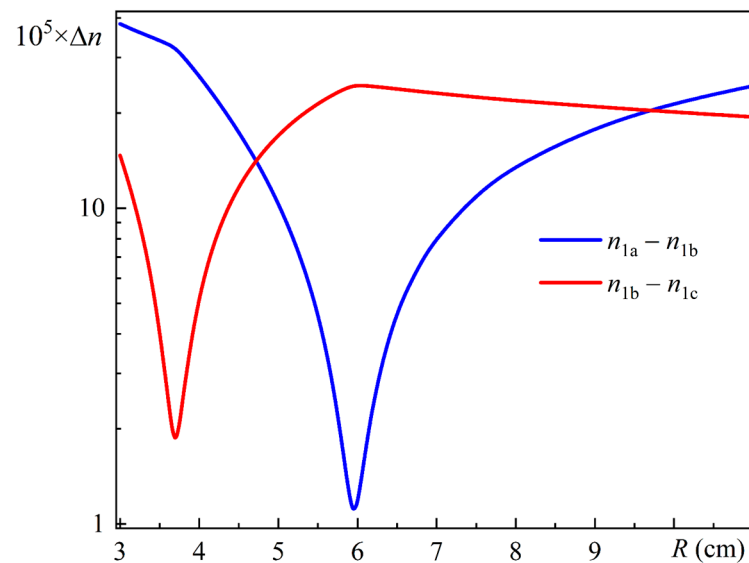

Figure 6. Differences in effective refractive index for different MOF-18 mode pairs versus bending radius *R*.

It is noteworthy that Modes 1a and 1b for a bending radius of 5.95 cm, as well as Modes 1b and 1c for a bending radius of 3.68 cm, are, in a sense, conditionally degenerate. This is due to the fact that they have strikingly similar spatial intensity distributions and also relatively close effective refractive indices. It is important to note, however, that the fundamental mode in an ordinary optical fiber is actually doubly degenerate in the classical sense, since it has two different (orthogonal) polarizations, identical spatial intensity distributions in the core, and the same values of the real parts of the effective refractive indices [41] (p. 30).

As illustrated in Figure 4, the difference in the effective refractive index for Modes 1a and 2a is less than 10^{-7} for bending radii exceeding 6.02 cm. For bending radii between 3.90 and 5.85 cm, the difference in the effective refractive index for Modes 1b and 2b is less than 10^{-7}. Similarly, for bending radii less than 3.40 cm, the difference in the effective refractive index for Modes 1c and 2c is less than 10^{-7}. Therefore, in the aforementioned bending radius ranges, the corresponding pairs of orthogonal modes may be considered degenerate in the classical sense.

As mentioned above, a detailed theoretical study of anticrossing and mode coupling in a bent LC MOF, such as that in [39], seems quite challenging. However, the spatial distributions of the electric (E) and magnetic (H) field components of different modes are of additional interest to understand these effects. We have studied the spatial distributions of the various components, such as E_x, E_y, E_z, H_x, H_y, and H_z. And we have found that for MOF-18, which is bent along the x-axis, only E_x and H_y have significant values (for modes polarized along the x-axis). The spatial distributions of E_x and H_y are quite similar to each other in terms of shape and differ from each other only in terms of absolute value. Therefore, for the purposes of illustration, we have selected the electric field components E_x of the different modes of MOF-18 at a number of bending radii, identical to those selected for Figure 5. Figure 7 shows spatial distributions of the electric field components E_x of Modes 1a and 1b for bending radii of 5.70 cm (a), 5.85 cm (b), 5.95 cm (c), 6.10 cm (d), and 6.25 cm (e). Legends for these figures are given in V/m.

As noted in the comments to Figure 6, the strongest coupling of Modes 1a and 1b is observed at the bending radius of MOF-18 around 5.95 cm, characterized by the smallest difference between their effective refractive indices (avoidance gap). We now turn to Figure 7c, which shows the spatial distributions of Modes 1a and 1b electric field components E_x for a 5.95 cm bending radius. As can be seen from this Figure 7c, the spatial distributions of electric field components E_x for Modes 1a and 1b are practically the same, both in terms of shape and in terms of absolute value. According to the authors of [39], the coupling between the different WGMs they studied is solely due to the boundary conditions of their components, which are integral parts of Maxwell's equations. Thus, it may be supposed that the observed agreement of the spatial distributions of the electric field components E_x for Modes 1a and 1b of MOF-18 indicates the maximum coupling of these modes at the given bending radius of 5.95 cm.

When the bending radius differs from 5.95 cm, differences appear in the spatial distributions of the electric field components E_x for Modes 1a and 1b (see Figure 7b,d, and then see Figure 7a,e). The integral of the overlap of the spatial distributions of the electric field components E_x for Modes 1a and 1b might offer some quantitative details regarding the coupling of these modes for different bending radii. Moreover, this integral may be more informative than the avoidance gap, which only indicates the presence of mode coupling. In addition, it may provide a more convincing physical confirmation of the coupling of the corresponding modes, in accordance with the results of [39]. But this is something that can be checked in the future, in the next work. It is also important to emphasize that the spatial distributions of the electric field components E_x for Modes 1a and 1b carry much more detailed information about these modes than, for example, their spatial intensity distributions. This can be seen by comparing Figures 7 and 5a.

Very similar spatial distributions of the electric field components E_x for Modes 1b and 1c are shown in Appendix A in Figure A1 for bending radii of 3.50 cm (a), 3.60 cm (b), 3.68 cm (c), 3.80 cm (d), and 3.90 cm (e).

Another interesting feature of the transformation of the MOF-18 modes can be observed if we refer to Figure 5 once again. As can be seen from Figure 5a, at a bending radius of 5.70 cm, Mode 1b has one additional intensity maximum in the ring gap, which is localized approximately on the x-axis. However, at a bending radius of 3.90 cm (see Figure 5b), Mode 1b has three additional maxima in the ring gap. Since it is difficult to follow the Mode 1b transformation from its intensity profiles in the bend radius interval between 5.70 cm and

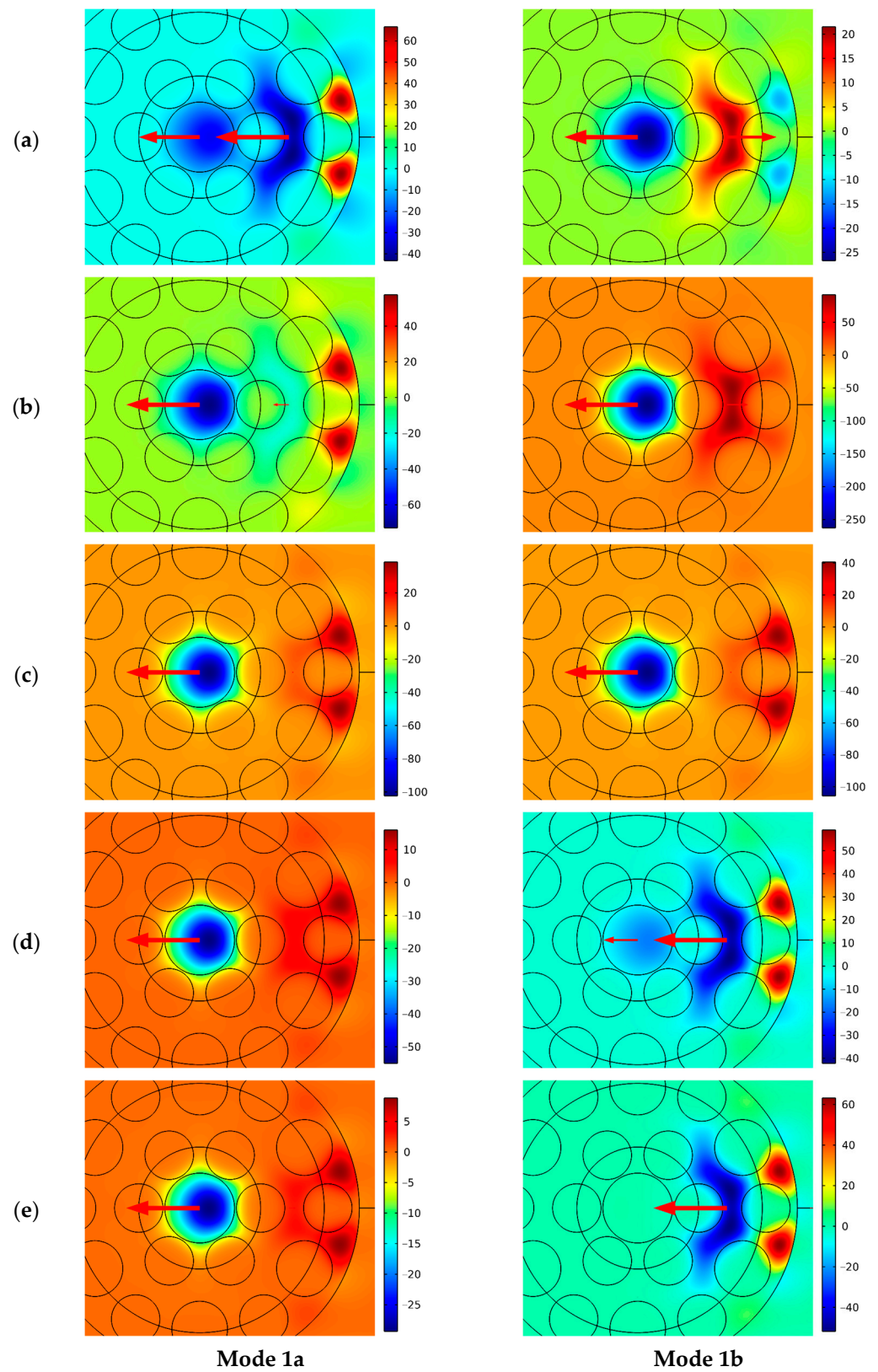3.90 cm, we used the spatial distributions of the electric field components E_x for Mode 1b for this purpose.

Figure 7. Spatial distributions of the electric field components E_x of Modes 1a and 1b for bending radii of 5.70 cm (**a**), 5.85 cm (**b**), 5.95 cm (**c**), 6.10 cm (**d**), and 6.25 cm (**e**).

Figure 8 shows the spatial distributions of the electric field components E_x of Mode 1b for bending radii of 4.10 cm (a), 4.50 cm (b), 4.90 cm (c), 5.30 cm (d), 5.50 cm (e), and 5.60 cm (f). From Figure 8, we can see the gradual transformation of Mode 1b of MOF-18 as the bending radius changes, especially in the ring gap.
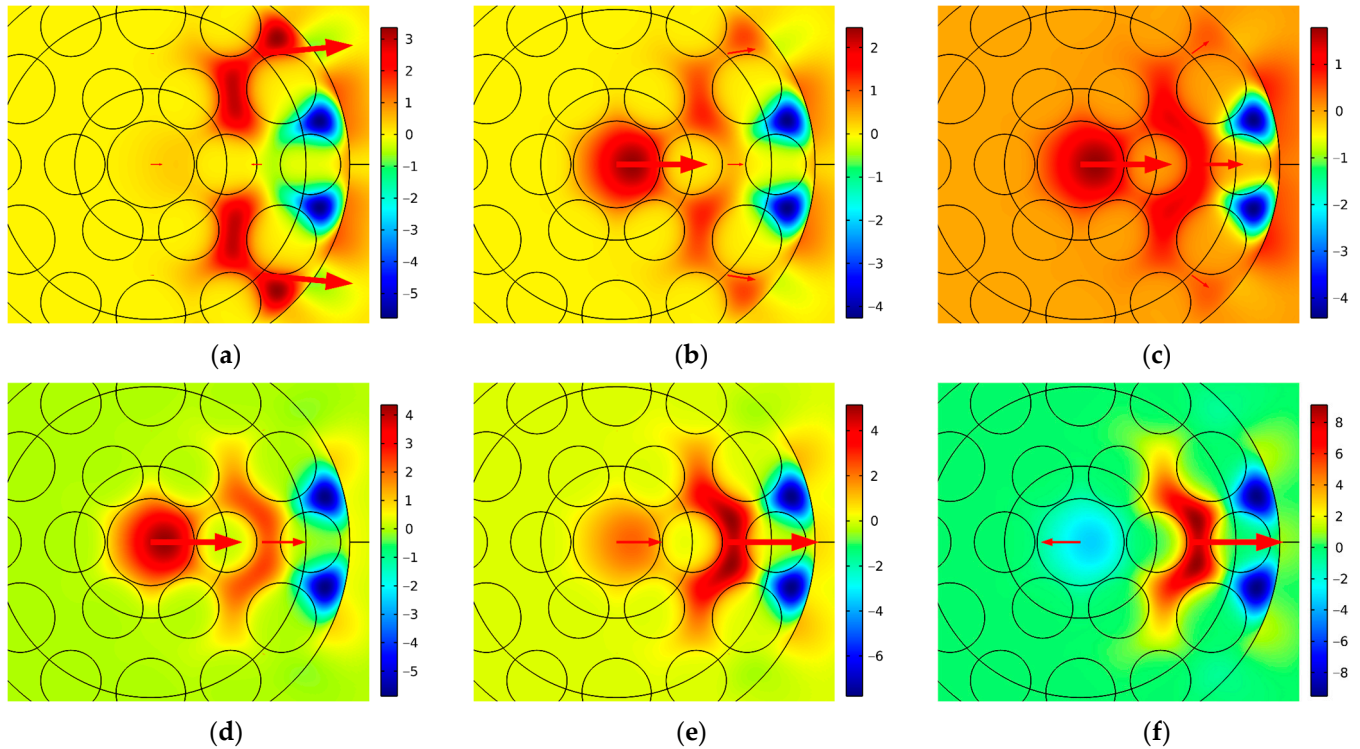

Figure 8. Spatial distributions of the electric field components E_x of Mode 1b for bending radii of 4.10 cm (**a**), 4.50 cm (**b**), 4.90 cm (**c**), 5.30 cm (**d**), 5.50 cm (**e**), and 5.60 cm (**f**).

For a more detailed quantitative study of transformations of the MOF-18 modes with changing bending radius, we determined the integral intensities of Modes 1a, 1b, and 1c in different regions of MBC-18: in the core, in the ring gap, and in the outer cladding. Figure 9 shows a schematic division of the MOF-18 cross section into different regions: the core (cor), indicated in blue; the ring gap (zaz), indicated in red; and the outer cladding (cla), indicated in green.

Figure 10a shows changes in the relative intensities of Modes 1a and 1b in the core (I_{1a_cor} and I_{1b_cor}), in the ring gap (I_{1a_zaz} and I_{1b_zaz}), and in the cladding (I_{1a_cla} and I_{1b_cla}), normalized by the sum for the corresponding mode for bending radii ranging from 5.0 cm to 7.0 cm. In addition, this figure shows two orange vertical lines indicating the bending radius range used to illustrate the spatial intensity distributions of Modes 1a and 1b in Figure 5a. From Figure 10a, we can see that the relative intensities of Modes 1a and 1b in the core, in the ring gap, and in the cladding of MOF-18 vary by about five orders of magnitude in the selected radius range. All corresponding values for Modes 1a and 1b coincide at about 5.95 cm bending radius. The variations in the relative intensities of Modes 1a and 1b in the core and in the ring gap have opposite characteristics of change.

As can be seen from Figure 5a, for a bending radius of 5.70 cm, the intensity of Mode 1a in the core of MOF-18 is minimal, rendering it nearly invisible in the figure, and Mode 1a resembles a mode of the cladding (mode of the ring gap). But Figure 10a demonstrates that the relative intensity of Mode 1a in the core has decreased to only 6% of its total intensity. Conversely, for this bending radius, the intensity of Mode 1b in the ring gap of MOF-18 is minimal, and this mode in Figure 5a resembles a fundamental mode. However, its relative intensity in the ring gap is significant, accounting for approximately 5% of its total intensity (see Figure 10a). A comparable picture is observed for a bending radius of 6.25 cm, but with

modes 1a and 1b reversed. Given that these changes occur within a narrow bending radius range, they can be conventionally described as a quasi-resonant transformation of modes.
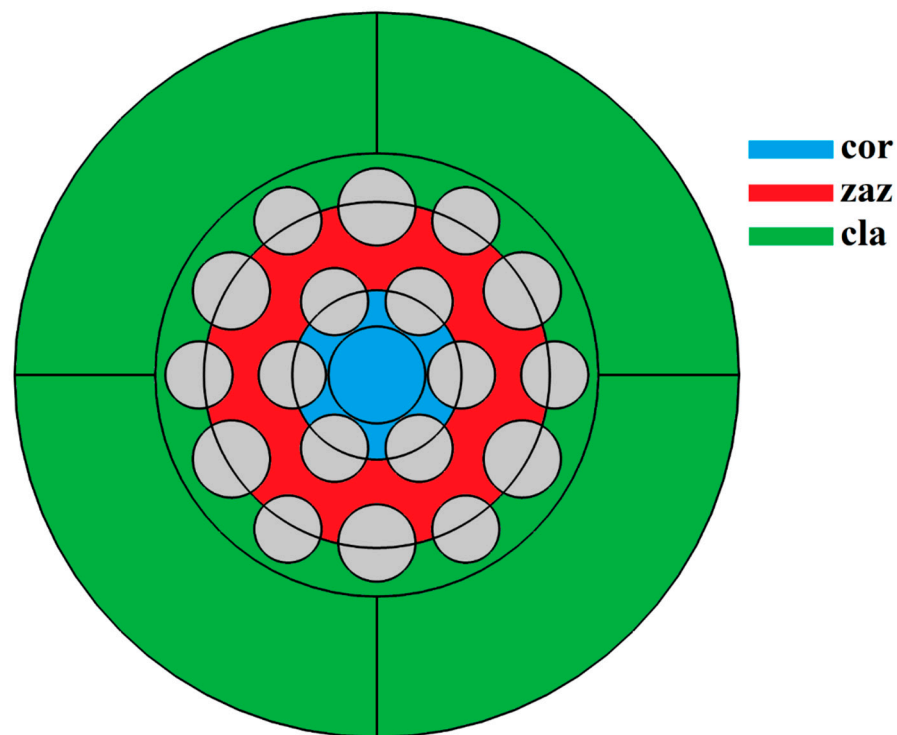

Figure 9. Schematic division of the MOF-18 cross section into different regions: core (cor), ring gap (zaz), and cladding (cla).

Furthermore, the relative intensities of Modes 1a and 1b in the cladding of MOF-18 vary by more than three orders of magnitude over the selected radius range and have dependencies very close to dependencies of Modes 1a and 1b leakage losses (α_{1a} and α_{1b}) on the bending radius. Figure 10b shows Modes 1a and 1b leakage losses and relative intensities in the cladding as a function of the bending radius in the range of 5.0 cm to 7.0 cm.

It should be noted that the calculations were performed up to a bending radius of 11 cm and showed good agreement. For this interval (from 5 to 11 cm), the ranges of variation in the loss of Mode 1a (α_{1a}) and its intensity in the cladding (I_{1a_cla}) were about five orders of magnitude. However, they are not shown in Figure 10b, simply to provide a more detailed illustration of these dependencies in a narrow interval of the bending radius. It is also worth noting that the coincidence of these dependencies is quite understandable from a physical point of view: losses in modes are determined by the fraction of their radiation that enters the outer cladding and, consequently, is lost.

Similar dependencies for Modes 1b and 1c are shown in Appendix A in Figure A2a,b for the 3.2–4.2 cm bending radius range.

Now consider the problem of determining the loss for radiation that is polarized along the *x*-axis and enters the MOF-18 segment of length *L* and bending radius *R*. Let us assume that a single-mode optical fiber with a pure silica glass core is used for the radiation entering MOF-18. This fiber has exactly the same core diameter (D_{core}) and the same bending radius, i.e., it is spliced with MOF-18 and wound together with it on a coil. The fundamental mode of this fiber, polarized along the *x*-axis, is Mode 1, according to the notations we have accepted (for this fiber it is the LP_{01} mode, polarized along the *x*-axis).

For simplicity, we assume that the spatial intensity distribution of Mode 1 has just the same form as the spatial intensity distributions of Modes 1a, 1b, and 1c in the core of MOF-18 but differs only in magnitude. In general, it is necessary to use the integral of the

overlap of spatial intensity distributions of corresponding modes to calculate the transition of intensity between fibers.
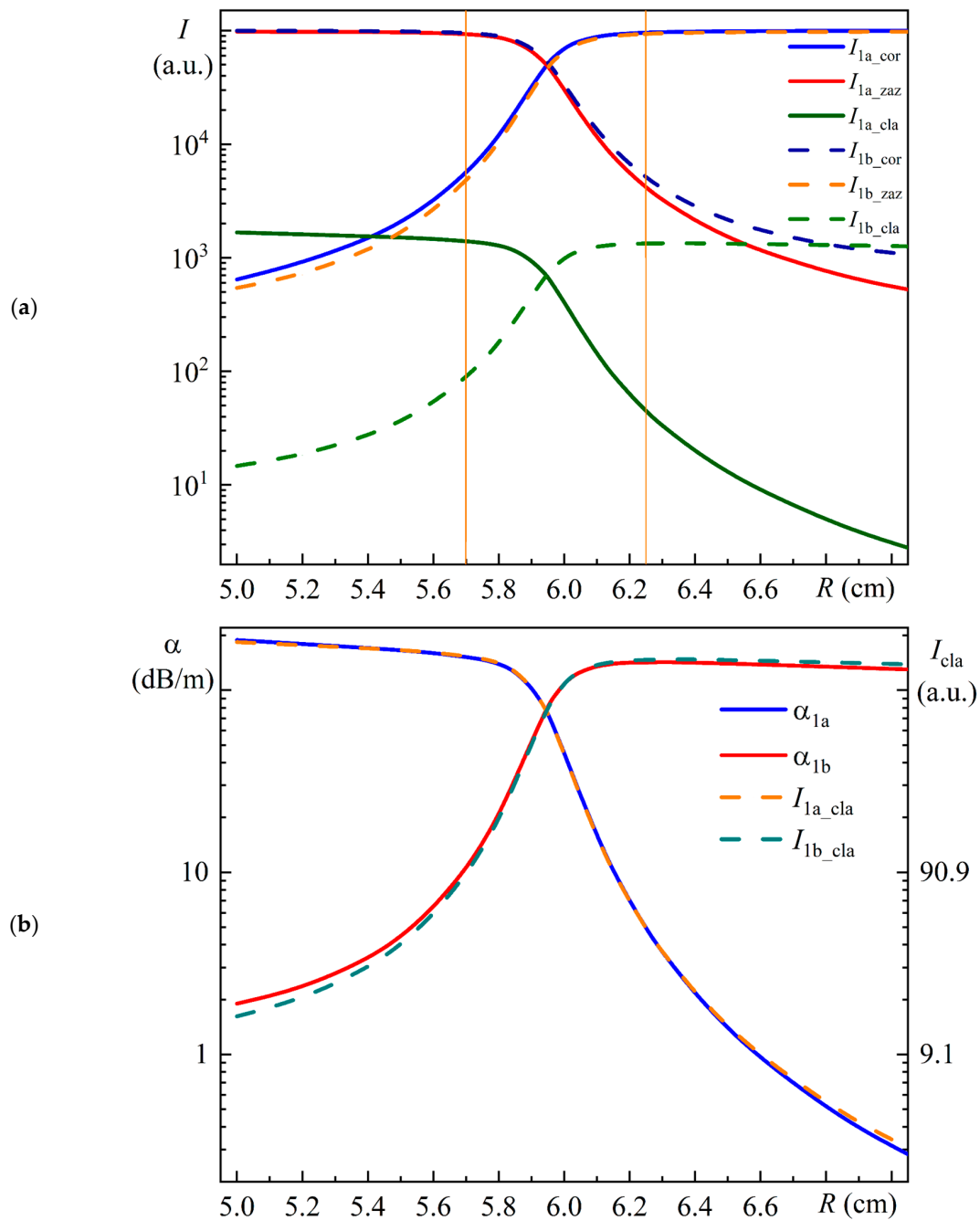

Figure 10. (**a**) Relative intensities of Modes 1a and 1b in the core (I_{1a_cor} and I_{1b_cor}), in the ring gap (I_{1a_zaz} and I_{1b_zaz}), and in the cladding (I_{1a_cla} and I_{1b_cla}) as a function of the bending radius; (**b**) dependencies of Modes 1a and 1b leakage losses (α_{1a} and α_{1b}) and the relative intensities in the cladding (I_{1a_cla} and I_{1b_cla}) on the bending radius.

Figure 11a shows the calculated dependence of the leakage losses α_{1a}, α_{1b}, and α_{1c} of Modes 1a, 1b, and 1c on the bending radius of MOF-18. In addition, this figure shows a 0.1 dB/m loss level to determine the edge of the single-mode range. In order to quantitatively describe the loss for radiation that enters MOF-18, we used the integrated intensities of Modes 1a, 1b, and 1c in the MOF-18 core, normalized by their sum, which are shown in Figure 11b. It is clear that for each particular radius, the incoming radiation is divided

between Modes 1a, 1b, and 1c of MOF-18 in proportion to their intensities in the core, that is, $I_{01} = I_{01a} + I_{01b} + I_{01c}$, where I_{01a}, I_{01b}, and I_{01c} are parts of I_{01}, defined by dependencies shown in Figure 11b. Then, when propagating along a segment of MOF-18 of length L, the intensity in each of these Modes 1a, 1b, and 1c will attenuate according to their respective inherent losses.
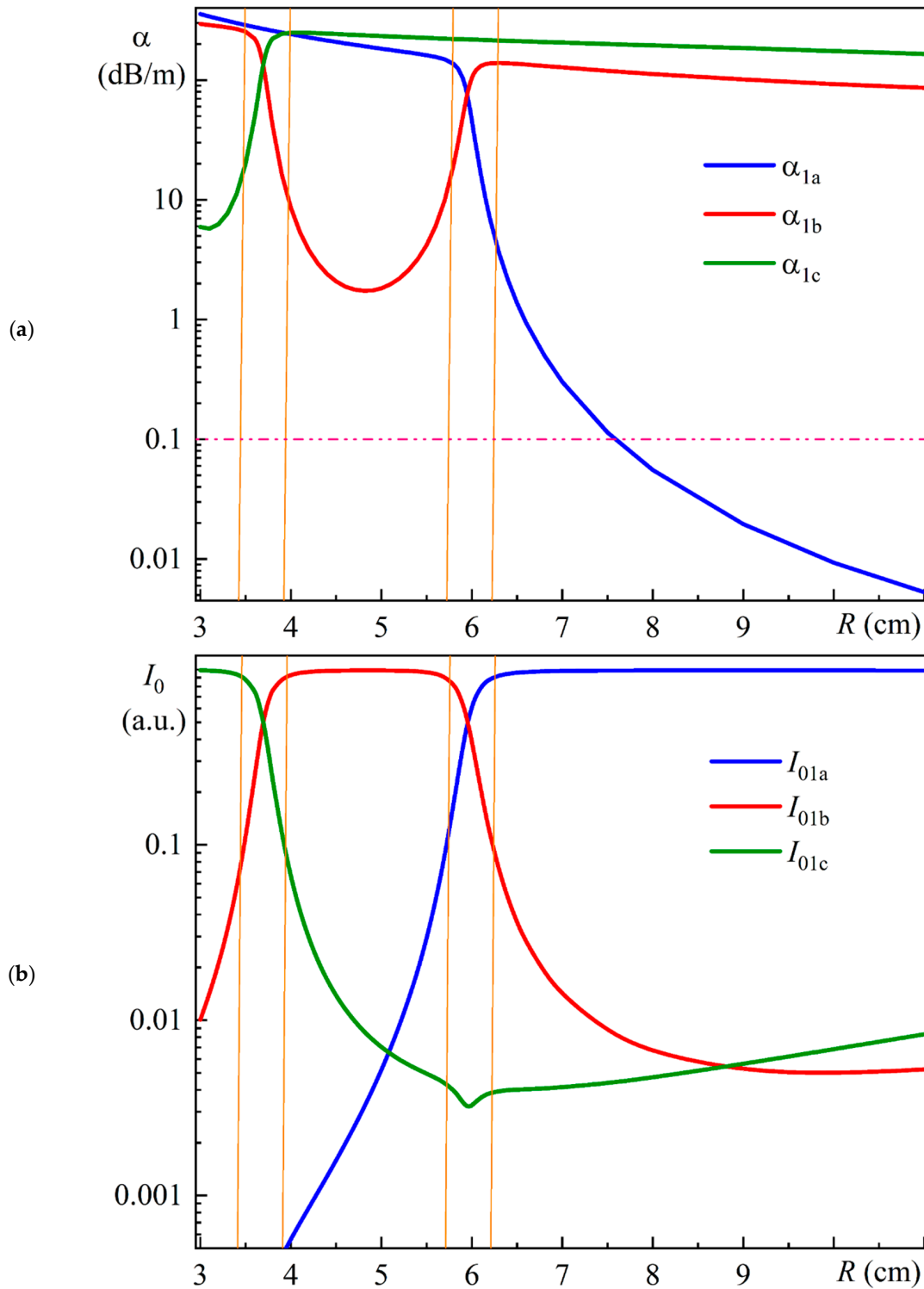

Figure 11. (**a**) Dependences of the leakage losses (α_{1a}, α_{1b}, and α_{1c}) of Modes 1a, 1b, and 1c on the bending radius of MOF-18; (**b**) dependences of the relative intensities (I_{01a}, I_{01b}, and I_{01c}) of Modes 1a, 1b, and 1c on the bending radius of MOF-18.

As a result, the total intensity of Mode 1, as a sum of Modes 1a, 1b, and 1c at the output of the MOF-18 segment with a length of L (which is also spliced with the mentioned single-mode optical fiber and wound together with MOF-18 on the coil), will be determined by the expression as follows:

$$I_1(L) = I_{1a}(L) + I_{1b}(L) + I_{1c}(L) = I_{01a} \cdot 10^{-\alpha(1a) \cdot L/10} + I_{01b} \cdot 10^{-\alpha(1b) \cdot L/10} + I_{01c} \cdot 10^{-\alpha(1c) \cdot L/10}. \tag{2}$$

Then, conventionally, we can determine the loss for Mode 1 using the following expression:

$$\alpha_1 = -(10/L) \cdot \log((I_{01a} \cdot 10^{-\alpha(1a) \cdot L/10} + I_{01b} \cdot 10^{-\alpha(1b) \cdot L/10} + I_{01c} \cdot 10^{-\alpha(1c) \cdot L/10})/(I_{01a} + I_{01b} + I_{01c})). \tag{3}$$

It should be emphasized that this expression for the loss of Mode 1 (in dB/m) depends on the length L of the MOF-18 segment, which should be taken into account when using this value in practice. Figure 12a shows the resulting losses for Mode 1 (α_1) at different MOF-18 segment lengths: 10 m and 2 m. Similar calculations were performed for radiation polarized along the y-axis, and the results of the calculations are very close because the initial values are close, as noted above. Figure 12b shows the resulting losses for Mode 1 (α_1) and Mode 2 (α_2) for MOF-18 segment length L = 10 m.

The resulting bending losses have two maxima at bending radii of 3.68 cm and 5.95 cm (see Figure 12b). Although these maxima are similar in shape to some resonance dependencies, the nature of these maxima is not resonance-like. In reality, this loss behavior is due to the presence of three modes: 1a, 1b, and 1c (as well as 2a, 2b, and 2c), which have sharp changes in their losses in opposite directions in a relatively narrow bending radius range near the corresponding values (5.95 cm for Modes 1a and 1b and 3.68 cm for Modes 1b and 1c; see Figure 11a). In addition, these modes also have sharp changes in their intensities in the MOF-18 core in the corresponding bending radius ranges (see Figure 11b). Thus, calculations of the losses for radiation propagating through MOF-18 using the rather simple Formulas (2) and (3) yield these intriguing results.

As can be seen from Figure 12a, for a bending radius R of less than 7 cm, the resulting loss dependencies are almost identical to the minimum losses for this range for the corresponding mode pairs, which can thus be used to approximate the resulting losses. On the other hand, for R greater than 7 cm, the resulting losses (in dB/m) become larger for the shorter length L of the MOF-18 segment. In order to explain this fact, we should refer to Figure 11b, which shows that in this range of bending radii (greater than 7 cm), the intensities of Modes 1b and 1c remain at a level that is quite noticeable. Simultaneously, Modes 1b and 1c have very large leakage losses (see Figure 11a).

As a result, the small fraction of intensity that enters these modes at the input to MOF-18 is almost completely lost over a very short section of it. Thus, when normalized to the length L of the MOF-18 segment, these losses have a greater effect on the final result (α_1 and α_2) for shorter lengths.

Another important observation from Figure 12a is that the correct consideration of the influence of Modes 1b and 1c allows us to determine a certain shift of the single-mode boundary towards larger values of the bending radius of MOF-18. This also makes it possible to determine more accurately the leakage loss at a bending radius of, for example, 8 cm, which turns out to be somewhat larger than if Modes 1b and 1c were not taken into account (i.e., for Mode 1a only). From Figure 12a, we can see that for the bending radius of 8 cm, the leakage loss for Mode 1a is 0.055 dB/m; the resulting loss for Mode 1 (α_1) for the MOF-18 segment lengths of 10 m is 0.060 dB/m; and for the MOF-18 segment lengths of 2 m, it is 0.080 dB/m.

The difference is therefore quite large, and this may be of significant importance both for practical applications and for the challenges of further optimizing the structure of MOF-18 for specific applications.
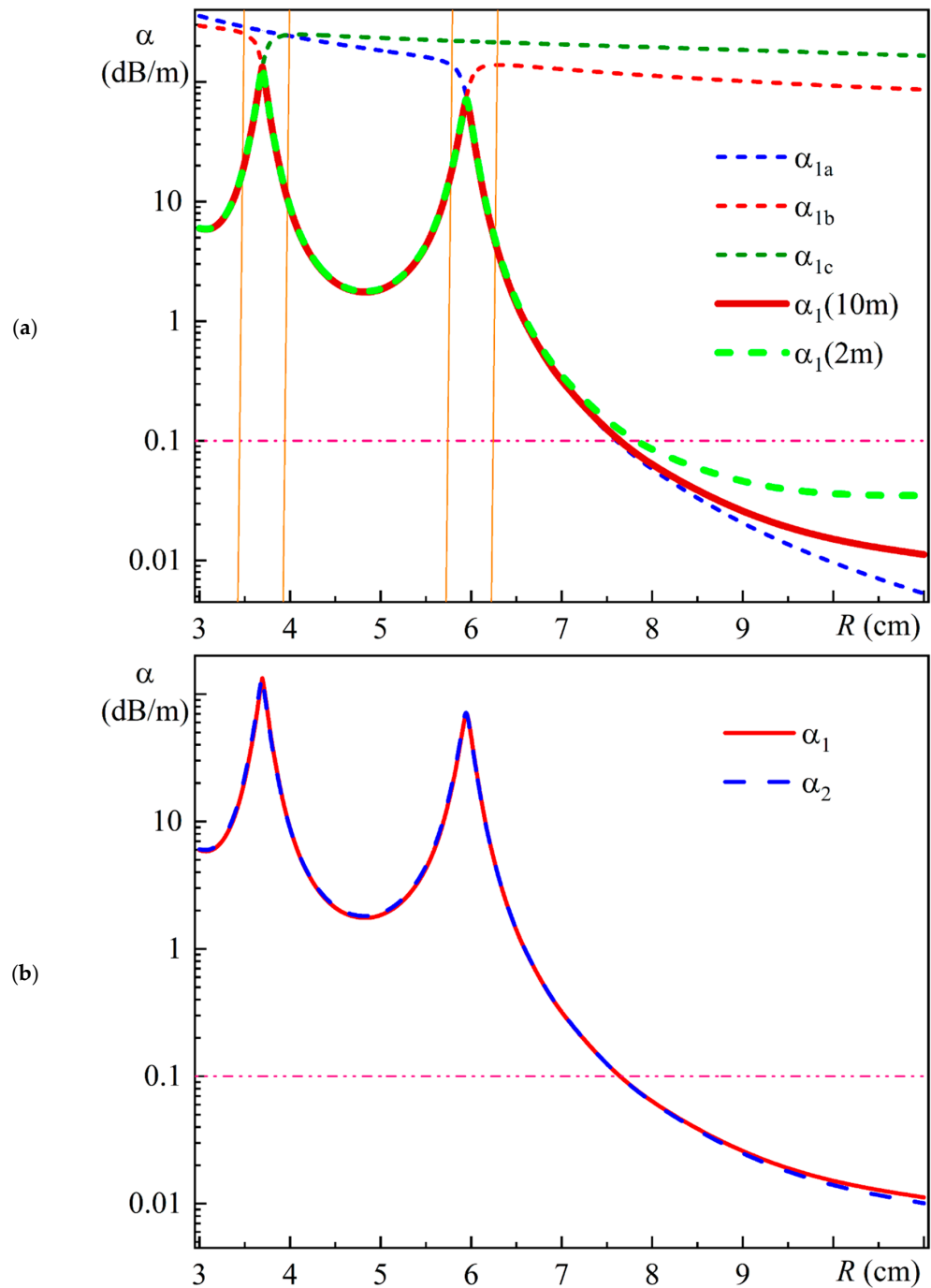
Figure 12. (**a**) Leakage loss dependences of Modes 1a, 1b, and 1c on MOF-18 bending radius as well as final loss α_1 for MOF-18 with lengths $L = 10$ m and $L = 2$ m; (**b**) MOF-18 leakage loss dependences on bending radius for radiation polarized along x-axis (α_1) and y-axis (α_2).

4. Discussion

In the present work, we have performed a detailed theoretical (numerical) study and analysis of the bending properties of all-glass LC MOFs across a range of bending radii from 3 cm to 11 cm. We have determined the spatial distributions of the electric field components of different modes in addition to the usual parameters, such as effective refractive indices, bending losses, and spatial intensity distributions, in order to achieve a physically accurate interpretation of the numerical results. We have also determined additional quantitative data, which are integral values of the intensities in three separate regions of the LC MOF: in the core, in the ring gap, and in the outer cladding.

A comprehensive analysis showed that three modes for each polarization must be considered to correctly calculate the bending losses. These modes cannot be attributed to either the fundamental core modes or the leaked cladding modes but are modes of the LC MOF as a whole. They have a complex spatial intensity distribution, with maxima both in the LC MOF core and in the ring gap between the element layers. Note that the ring gap maxima have different shapes for different modes. Two pairs of these three modes are coupled in two different bending radius ranges. Modes 1a and 1b have the strongest coupling for the bending radius near 5.95 cm (see Figures 6 and 7c), and Modes 1b and 1c have the strongest coupling for the bending radius near 3.68 cm (see Figures 6 and A1c). Thus, we can conclude that the coupling of these mode pairs is resonant in nature.

It should be emphasized that this conclusion has a clear physical meaning, which differs from the widely accepted hypothesis of the coupling of the fundamental core mode with leaked cladding modes.

The resulting bending losses of the LC MOF have two maxima at bending radii of 3.68 cm and 5.95 cm, but the nature of these maxima is not resonant; they are due to the joint influence of all three modes, each of which has specific dependencies of its loss and intensity on the bending radius, exhibiting quasi-resonant behavior near the corresponding bending radii.

Thus, we can conclude that the observed coincidence of the positions of the loss maxima with those of the maximum strong coupling in the mode pairings indicates an underlying relationship between the LC MOF properties, and this relationship is fully consistent with the causality principle.

It is worth highlighting some unique features of the LC MOF because it is a leaky channel fiber, i.e., by definition, it has non-zero leakage losses for the fundamental modes, so that the field of these modes extends beyond the core. In addition, LC MOF cladding elements are made of fluorine-doped silica glass. Their refractive index is only a few thousandths less than that of pure silica glass. It is likely that this is responsible for some of the properties of the LC MOF mentioned above. On the other hand, these properties may be more pronounced in the LC MOF because of its unique properties, but they may also be found in some other optical fibers when they are more widely studied.

For example, as mentioned in the Introduction, for the negative-curvature hollow-core chalcogenide fiber described in [22], the authors found two maxima in the bending losses for each of the two polarizations of the fundamental mode. However, the authors gave dependencies of the real parts of the effective refractive indices on the bending radius for six modes, with three modes for each of the two polarizations. But they did not present the bending-loss dependencies for all of these modes and did not explain how they obtained only two bending-loss dependencies on bending radius for a total of six modes.

Taking into account the results obtained in the present work, it can be assumed that the approach proposed by us would help to obtain more convincing results for this optical fiber. For this purpose, it would be necessary to determine the bending-loss dependencies for all six modes found in [22] and also the evolution of the spatial distributions of intensities of all these modes with changing radii, as well as the bending dependencies of the integral intensities of these modes in the core of the fiber. Then, using Formulas (2) and (3) for loss calculations for radiation propagating through the fiber, it is possible to determine the real bending-loss dependencies of this optical fiber for each of the two polarizations. From the evolution of the spatial distributions of the intensities of the modes with changing radii, it can be concluded that there are two pairs of modes in three modes for each of the polarizations, coupled in two different bending radius ranges. This conclusion will have a clear physical meaning that differs from the widely accepted hypothesis about the coupling of the fundamental core mode with some tube modes.

We are confident that our proposed approach will contribute to the generation of more compelling results for other optical fibers as their research is expanded.

Another interesting question is how these three Modes 1a, 1b, and 1c (and also Modes 2a, 2b, and 2c) should be named, since their parameters vary with the bending radii, including changes in the spatial intensity distributions between different regions of the LC

MOF (see Figures 9, 10a and A2a). Although such a conventional term as "mixed mode" can be found in the literature [26], it has no physical justification and therefore cannot be used.

A very original variant of fundamental mode selection was proposed in [43]. In this paper, the authors investigated anticrossings (avoided crossings) in a so-called large-pitch photonic crystal fiber (LPF). For this LPF, the authors of [43] discovered a group of modes with Gaussian intensity distribution in the core of the fiber. The mode in the group that had the maximum value of integral intensity in the core was selected as the fundamental mode (FM) [43]. Other modes from this group were called HOMs. It should be emphasized that such a choice of the fundamental mode resulted in a very unusual dependence of its effective refractive index on the bending radius of this photonic crystal fiber. This dependence had some discontinuities at some radius values, and simultaneously for these radius values the so-called FMs had significant intensities in the cladding [43].

It is obvious that this kind of renaming does not add anything constructive to our understanding of the physical picture. Concurrently, this endeavor illustrates that the issue of designation for modes is also pertinent to other types of optical fibers and remains unresolved. Therefore, for the time being, we will continue to refer to these modes by simple numbers and letters.

We believe that the detailed theoretical (numerical) investigations carried out in our work will be of great value in the studies of many other MOFs where details remain unclear.

5. Conclusions

A detailed theoretical study of the bending properties of the original all-glass leakage channel microstructured optical fiber (LC MOF) presented in this paper was performed over a bending radius range from 3 cm to 11 cm. The spatial distributions of the electric field components of different modes in addition to the usual parameters, such as effective refractive indices, bending losses, and spatial intensity distributions, were determined. A detailed analysis showed that in order to correctly calculate bending losses, three actual modes for each polarization must be taken into account. Two pairs of these three modes are coupled in two different bending radius ranges: near 3.68 cm and near 5.95 cm. And these pairs have sharply changed avoidance gaps (differences between the effective refractive indices of the respective modes) with minima at the corresponding bending radii. Thus, it can be concluded that the mode coupling in these pairs is resonant. The resulting bending losses of LC MOF for two polarizations have two maxima at bending radii of 3.68 cm and 5.95 cm, but the nature of these maxima is not resonant. In fact, this loss behavior is due to the presence of three modes for each polarization, two pairs of which have sharply varying losses and intensities in relatively narrow ranges of bending radii close to their respective values, that is, they exhibit quasi-resonant behavior near the corresponding bending radii. Simple loss calculations for radiation propagating through the LC MOF using Formulas (2) and (3) give such intriguing results. The observed coincidence of the positions of the loss maxima with those of the maximum strong coupling in the mode pairings indicates the underlying relationship between the LC MOF properties. This relationship is fully consistent with the causality principle.

Author Contributions: Conceptualization, A.N.D. and S.L.S.; methodology, A.N.D., S.L.S.; software, A.N.D. and V.V.D.; validation, A.N.D., V.V.D. and S.L.S.; formal analysis, A.N.D., V.V.D. and S.L.S.; investigation, A.N.D.; resources, S.L.S.; data curation, A.N.D.; writing—original draft preparation, A.N.D.; writing—review and editing, A.N.D., V.V.D. and S.L.S.; visualization, A.N.D.; supervision, S.L.S.; project administration, S.L.S.; funding acquisition, S.L.S. All authors have read and agreed to the published version of the manuscript.

Institutional Review Board Statement: Not applicable.

Informed Consent Statement: Not applicable.

Data Availability Statement: Data are contained within the article.

Conflicts of Interest: The authors declare no conflicts of interest.
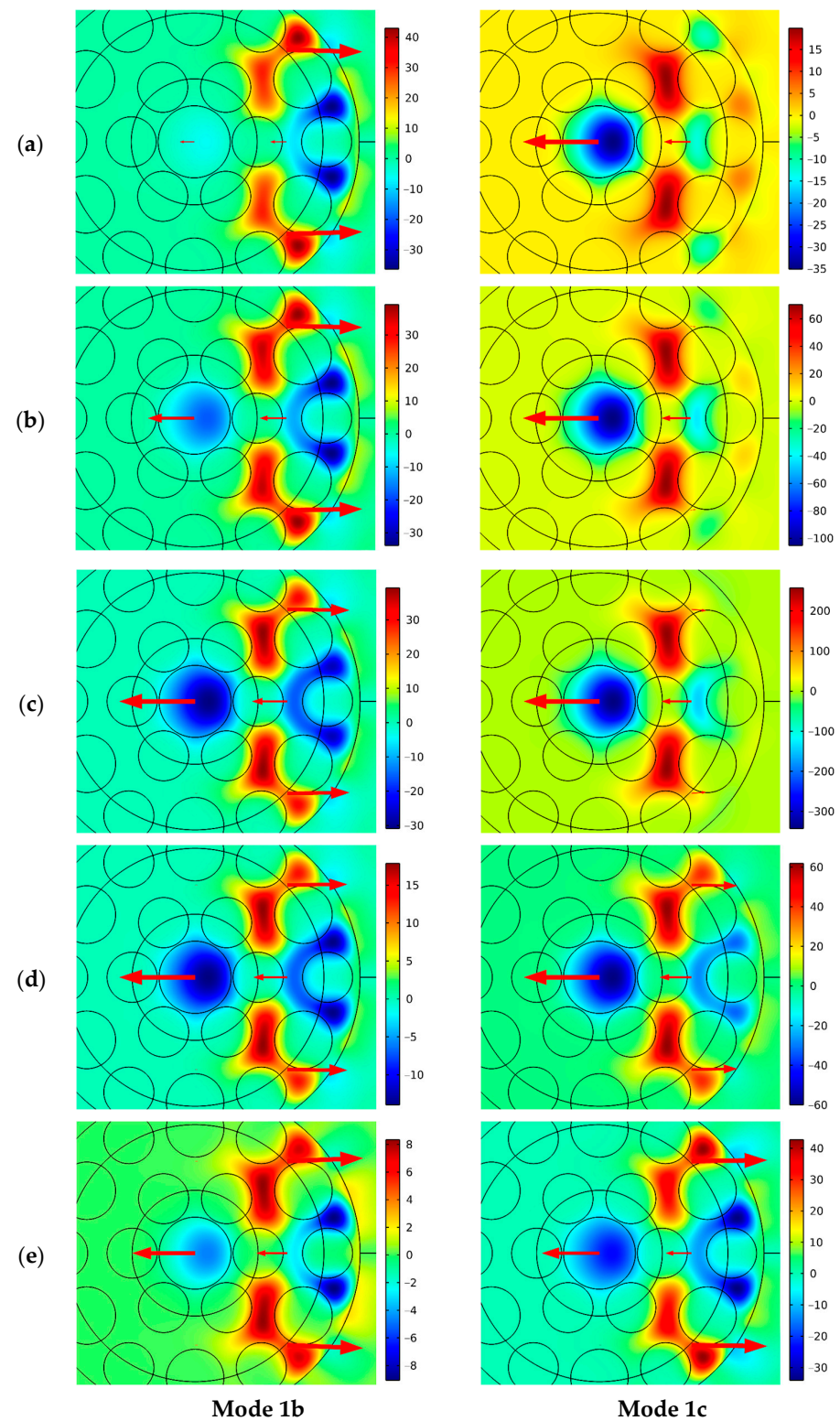
Appendix A

Figure A1. Spatial distributions of the electric field components E_x of Modes 1b and 1c for bending radii of 3.50 cm (**a**), 3.60 cm (**b**), 3.68 cm (**c**), 3.80 cm (**d**), and 3.90 cm (**e**).
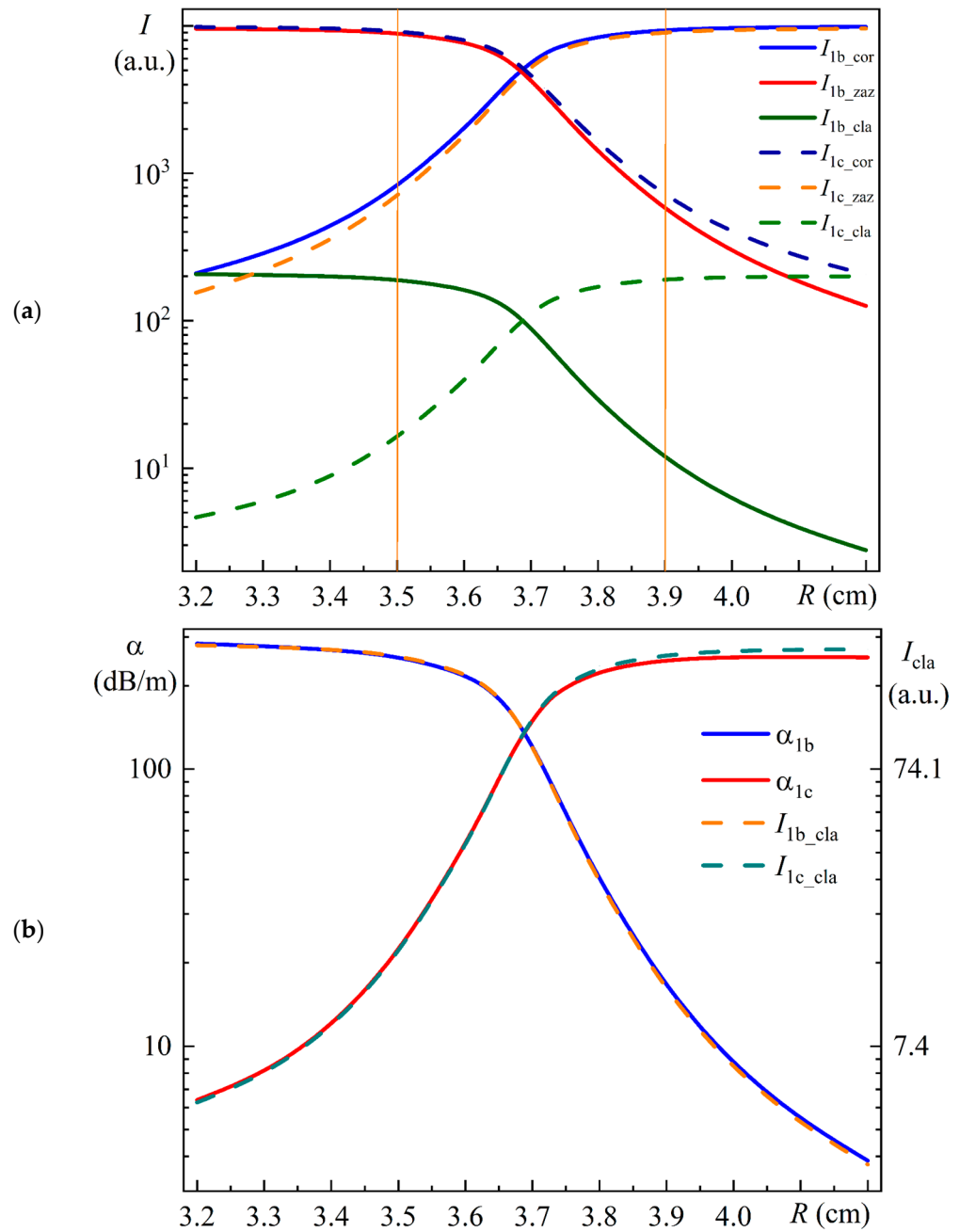
Figure A2. (**a**) Relative intensities of Modes 1b and 1c in the core (I_{1b_cor} and I_{1c_cor}), in the ring gap (I_{1b_zaz} and I_{1c_zaz}), and in the cladding (I_{1b_cla} and I_{1c_cla}) as a function of the bending radius; (**b**) dependencies of Modes 1b and 1c leakage losses (α_{1b} and α_{1c}) and the relative intensities in the cladding (I_{1b_cla} and I_{1c_cla}) on the bending radius.

References

1. Kong, F.; Gu, G.; Hawkins, T.W.; Jones, M.; Parsons, J.; Kalichevsky-Dong, M.T.; Pulford, B.; Dajani, I.; Dong, L. ~1 kilowatt Ytterbium-doped all-solid photonic bandgap fiber laser. *Proc. SPIE* **2017**, *10083*, 1008311.
2. Ikoma, S.; Nguyen, H.K.; Kashiwagi, M.; Uchiyama, K.; Shima, K.; Tanaka, D. 3 kW single stage all-fiber Yb-doped single-mode fiber laser for highly reflective and highly thermal conductive materials processing. *Proc. SPIE* **2017**, *10083*, 100830Y.
3. Jollivet, C.; Bradford, J.; Conroy, M.; Carter, A.; Tankala, K. Next Generation of DC fibers enabling high performance and reliability of industrial fiber lasers beyond 1.5kW levels. *Proc. SPIE* **2019**, *11206*, 1120605.
4. Platonov, N.; Yagodkin, R.; Cruz, J.D.L.; Gapontsev, V. Single-mode 3kW Ytterbium fiber amplifier with diffraction-limited divergence in all-fiber format and compact modular package. *Proc. SPIE* **2021**, *11665*, 1166505.
5. Pulford, B.; Holten, R.; Matniyaz, T.; Kalichevsky-Dong, M.T.; Hawkins, T.W.; Dong, L. kW-level monolithic single-mode narrow-linewidth all-solid photonic bandgap fiber amplifier. *Opt. Lett.* **2021**, *46*, 4458–4461. [CrossRef]

6. Egorova, O.N.; Semjonov, S.L.; Kosolapov, A.F.; Denisov, A.N.; Pryamikov, A.D.; Gaponov, D.A.; Biriukov, A.S.; Dianov, E.M.; Salganskii, M.Y.; Khopin, V.F.; et al. Single-mode all-silica photonic bandgap fiber with 20-μm mode-field diameter. *Opt. Express* **2008**, *16*, 11735–11740. [CrossRef]
7. Kashiwagi, M.; Saitoh, K.; Takenaga, K.; Tanigawa, S.; Matsuo, S.; Fujimaki, M. Effectively single-mode all-solid photonic bandgap fiber with large effective area and low bending loss for compact high-power all-fiber lasers. *Opt. Express* **2012**, *20*, 15061–15070. [CrossRef]
8. Matniyaz, T.; Li, W.; Kalichevsky-Dong, M.; Hawkins, T.W.; Parsons, J.; Gu, G.; Dong, L. Highly efficient cladding-pumped single-mode three-level Yb all-solid photonic bandgap fiber lasers. *Opt. Lett.* **2019**, *44*, 807–810. [CrossRef]
9. Février, S.; Jamier, R.; Blondy, J.-M.; Semjonov, S.L.; Likhachev, M.E.; Bubnov, M.M.; Dianov, E.M.; Khopin, V.F.; Salganskii, M.Y.; Guryanov, A.N. Low-loss singlemode large mode area all-silica photonic bandgap fiber. *Opt. Express* **2006**, *14*, 562–569. [CrossRef]
10. Aleshkina, S.S.; Likhachev, M.E.; Pryamikov, A.D.; Gaponov, D.A.; Denisov, A.N.; Bubnov, M.M.; Salganskii, M.Y.; Laptev, A.Y.; Guryanov, A.N.; Uspenskii, Y.A.; et al. Very-large-mode-area photonic bandgap Bragg fiber polarizing in a wide spectral range. *Opt. Lett.* **2011**, *36*, 3566–3568. [CrossRef]
11. Vanvincq, O.; Habert, R.; Cassez, A.; Baudelle, K.; Labat, D.; Delobel, S.; Quiquempois, Y.; Bouwmans, G.; Bigot, L. Polarization-maintaining and single-mode large mode area pixelated Bragg fiber. *Opt. Lett.* **2020**, *45*, 1946–1949. [CrossRef] [PubMed]
12. Wong, W.S.; Peng, X.; McLaughlin, J.M.; Dong, L. Breaking the limit of maximum effective area for robust single-mode propagation in optical fibers. *Opt. Lett.* **2005**, *30*, 2855–2857. [CrossRef] [PubMed]
13. Dong, L.; Peng, X.; Li, J. Leakage channel optical fibers with large effective area. *J. Opt. Soc. Am. B* **2007**, *24*, 1689–1697. [CrossRef]
14. Gu, G.; Kong, F.; Hawkins, T.W.; Foy, P.; Wei, K.; Samson, B.; Dong, L. Impact of fiber outer boundaries on leaky mode losses in leakage channel fibers. *Opt. Express* **2013**, *21*, 24039–24048. [CrossRef]
15. Saitoh, K.; Tsuchida, Y.; Rosa, L.; Koshiba, M.; Poli, F.; Cucinotta, A.; Selleri, S.; Pal, M.; Paul, M.; Ghosh, D.; et al. Design of all-solid leakage channel fibers with large mode area and low bending loss. *Opt. Express* **2009**, *17*, 4913–4919. [CrossRef]
16. Dong, L.; Wu, T.; Mckay, H.A.; Fu, L.; Li, J.; Winful, H.G. All-glass large-core leakage channel fibers. *IEEE J. Sel. Top. Quantum Electron.* **2009**, *15*, 47–53. [CrossRef]
17. Denisov, A.N.; Semjonov, S.L. All-glass single-mode microstructured optical fibres with a large-diameter core and low bending losses. *Quantum Electron.* **2021**, *51*, 1081–1089. [CrossRef]
18. Denisov, A.; Dvoyrin, V.; Kosolapov, A.; Likhachev, M.; Velmiskin, V.; Zhuravlev, S.; Semjonov, S. All-Glass Single-Mode Leakage Channel Microstructured Optical Fibers with Large Mode Area and Low Bending Loss. *Photonics* **2023**, *10*, 465. [CrossRef]
19. Nicholson, J.W.; DeSantolo, A.; Windeler, R.S.; Monberg, E.; Lukonin, V.; Pincha, J.; Hariharan, A.; Xu, X.; Williams, G.; Goldberg, Z.; et al. Next generation Yb-doped fibers for high-power, narrow-linewidth lasers. *Proc. SPIE* **2022**, *11981*, 119810R.
20. Rosales-Garcia, A.; Jensen, R.; Ovtar, S.; Ingerslev, K.; Edvold, B.; Kristensen, P.; Nicholson, J.W.; DiGiovanni, D.J.; Pálsdóttir, B. Photodarkening-free fiber laser based on Yb-doped 20/400 gain fiber. *Proc. SPIE* **2022**, *11981*, 119810W.
21. Olszewski, J.; Szpulak, M.; Urbanczyk, W. Effect of coupling between fundamental and cladding modes on bending losses in photonic crystal fibers. *Opt. Express* **2005**, *13*, 6015–6022. [CrossRef] [PubMed]
22. Wei, C.; Menyuk, C.R.; Hu, J. Bending-induced mode non-degeneracy and coupling in chalcogenide negative curvature fibers. *Opt. Express* **2016**, *24*, 12228–12239. [CrossRef] [PubMed]
23. He, L.; Liang, Y.; Guan, Y.; Gu, Z.; Xia, K.; Wang, X.; Dai, S.; Shen, X.; Liu, Z. Large mode-area all-solid anti-resonant fiber based on chalcogenide glass for mid-infrared transmission. *Opt. Express* **2023**, *31*, 8975–8986. [CrossRef] [PubMed]
24. Saitoh, K.; Varshney, S.; Sasaki, K.; Rosa, L.; Pal, M.; Paul, M.C.; Ghosh, D.; Bhadra, S.K.; Koshiba, M. Limitation on Effective Area of Bent Large-Mode-Area Leakage Channel Fibers. *J. Lightwave Technol.* **2011**, *29*, 2609–2615. [CrossRef]
25. Barankov, R.A.; Wei, K.; Samson, B.; Ramachandran, S. Resonant bend loss in leakage channel fibers. *Opt. Lett.* **2012**, *37*, 3147–3149. [CrossRef] [PubMed]
26. Fini, J.M. Design of solid and microstructure fibers for suppression of higher-order modes. *Opt. Express* **2005**, *13*, 3477–3490. [CrossRef]
27. Tsuchida, Y.; Saitoh, K.; Koshiba, M. Design of single-moded holey fibers with large-mode-area and low bending losses: The significance of the ring-core region. *Opt. Express* **2007**, *15*, 1794–1803. [CrossRef]
28. Kogelnik, H.; Shank, C.V. Coupled-Wave Theory of Distributed Feedback Lasers. *J. Appl. Phys.* **1972**, *43*, 2327–2335. [CrossRef]
29. Yariv, A. Coupled-mode theory for guided-wave optics. *IEEE J. Quantum Electron.* **1973**, *9*, 919–933. [CrossRef]
30. Winick, K.A. Effective-index method and coupled-mode theory for almost-periodic waveguide gratings: A comparison. *Appl. Opt.* **1992**, *31*, 757–764. [CrossRef]
31. de Sterke, C.M.; Broderick, N.G.R. Coupled-mode equations for periodic super-structure Bragg gratings. *Opt. Lett.* **1995**, *20*, 2039–2041. [CrossRef] [PubMed]
32. McCall, M. On the Application of Coupled Mode Theory for Modeling Fiber Bragg Gratings. *J. Lightwave Technol.* **2000**, *18*, 236–242. [CrossRef]
33. Koyamada, Y. Analysis of Core-Mode to Radiation-Mode Coupling in Fiber Bragg Gratings with Finite Cladding Radius. *J. Lightwave Technol.* **2000**, *18*, 1220–1225. [CrossRef]
34. Song, N.; Mu, J.; Huang, W.P. Application of the Complex Coupled-Mode Theory to Optical Fiber Grating Structures. *J. Lightwave Technol.* **2010**, *28*, 761–767. [CrossRef]

35. Fujisawa, T.; Koshiba, M. Analysis of photonic crystal waveguide gratings with coupled-mode theory and a finite-element method. *Appl. Opt.* **2006**, *45*, 4114–4121. [CrossRef]
36. He, Z.; Zhu, Y.; Kaňka, J.; Du, H. Core-cladding mode coupling and recoupling in photonic crystal fiber for enhanced overlap of evanescent field using long-period gratings. *Opt. Express* **2010**, *18*, 507–512. [CrossRef]
37. Olivier, S.; Benisty, H.; Weisbuch, C.; Smith, C.J.M.; Krauss, T.F.; Houdré, R. Coupled-mode theory and propagation losses in photonic crystal waveguides. *Opt. Express* **2003**, *11*, 1490–1496. [CrossRef]
38. Wu, T.; Lalanne, P. Exact Maxwell evolution equation of resonator dynamics: Temporal coupled-mode theory revisited. *Opt. Express* **2024**, *32*, 20904–20914. [CrossRef]
39. Werner, C.S.; Sturman, B.; Podivilov, E.; Manjeshwar, S.K.; Buse, K.; Breunig, I. Control of mode anticrossings in whispering gallery microresonators. *Opt. Express* **2018**, *26*, 762–771. [CrossRef]
40. Rashidi, K.; Mirjalili, S.M.; Taleb, H.; Fathi, D. Optimal Design of Large Mode Area Photonic Crystal Fibers Using a Multiobjective Gray Wolf Optimization Technique. *J. Lightwave Technol.* **2018**, *36*, 5626–5632. [CrossRef]
41. Agrawal, G. *Nonlinear Fiber Optics*, 4th ed.; Academic Press: New York, NY, USA, 2007.
42. Tsuchida, Y.; Saitoh, K.; Koshiba, M. Design and characterization of single-mode holey fibers with low bending losses. *Opt. Express* **2005**, *13*, 4770–4779. [CrossRef] [PubMed]
43. Jansen, F.; Stutzki, F.; Jauregui, C.; Limpert, J.; Tünnermann, A. Avoided crossings in photonic crystal fibers. *Opt. Express* **2011**, *19*, 13578–13589. [CrossRef] [PubMed]